GEOPHYSICS, VOL. 80, NO. 3 (MAY-JUNE 2015); P. R123–R138, 17 FIGS., 1 TABLE.
10.1190/GEO2014-0193.1

Imaging blended vertical seismic profiling data using full-wavefield migration in the common-receiver domain

A. K. Soni[1] and D. J. Verschuur[2]

ABSTRACT

For vertical-seismic-profiling (VSP) measurements, the use of blended acquisition, with time-overlapping shot records, can greatly reduce the downtime and, thereby, provide large cost savings. For directly imaging blended VSP measurements, we have used full-wavefield migration (FWM). FWM is an inversion-based imaging scheme that enables us to use any kind of complex source wavefield to estimate the subsurface reflectivity, using all the multiples (surface and internal) in the recorded data. The multiple scattering helps in improving the illumination as well as the vertical resolution of the image. In this scheme, active deblending is not required because the imaging process itself acts as a deblending procedure. We tested the potential of FWM to image blended VSP data, using simple and complex synthetic models. We clearly determined that using the primaries, surface multiples, and internal multiples enhanced the illumination away from the well trajectory, in which blending noise was suppressed due to the inversion scheme. We observed that some blending crosstalk noise leaked into the images with large blending factors. Such noise could be further reduced with additional constraints in the involved least-squares inversion process.

INTRODUCTION

In conventional seismic data acquisition, the time interval between firing two consecutive shots is sufficiently large to avoid overlap in the responses. On the other hand, in blended-source seismic data acquisition (also called *simultaneous source acquisition*), the time interval between firing two or more shots is relatively small, and therefore, the wavefields recorded have interference noise. Blended acquisition (Beasley et al., 1998; Bagaini, 2006; Ikelle, 2007; Stefani et al., 2007; Berkhout, 2008; Berkhout et al., 2008; Blacquiere et al., 2009) in the surface seismic case is slowly becoming a routine practice in the oil and gas industry. Blending in surface seismic has made huge 3D surveys possible within economical survey times. It has been proven to improve the quality as well as the economic aspects by reducing the cost of data acquisition and survey time, while still acquiring dense surveys (see, e.g., Berkhout, 2008; Howe et al., 2008; Bouska, 2010; Berkhout et al., 2012; Doulgeris, 2013).

Recently, proposals to acquire 3D vertical-seismic-profiling (VSP) data using simultaneous sources to reduce the borehole acquisition cost significantly (Gulati et al., 2011). As we know, VSP data acquisition requires us to stop well production to reduce disruption and noises, and therefore, it is associated with costly rig downtime. Thus, reducing downtime via blended source acquisition is of great importance. Nawaz and Borland (2013) discuss the processing sequence for simultaneous source 3D-VSP data. In a similar way, Morley (2013) discuss the application of compressed sensing in 3D-VSP acquisition and processing.

For the processing, imaging, and (full-waveform) inversion of the blended source data, we have seen methods of deblending the sources from the acquired seismic data (Moore et al., 2008; Spitz et al., 2008; Huo et al., 2009; Kim et al., 2009; Ayeni et al., 2011; Doulgeris et al., 2011, 2012; Mahdad et al., 2011a, 2012; Beasley et al., 2012; van Borselen et al., 2012; Wapenaar et al., 2012). The deblended data, i.e., the separated shot records, can be fed into the conventional processing and imaging methods. On the other hand, there have been investigations in performing processing (e.g., van Groenestijn and Verschuur, 2011; Bagaini et al., 2012; Hou et al., 2012), imaging (e.g., Tang and Biondi, 2009; Verschuur and Berkhout, 2009, 2011; Jiang and Abma, 2010; Berkhout et al., 2012; Dai et al., 2012; Huang and Schuster, 2012; Godwin and Sava, 2013), and inversion (e.g., Ayeni et al., 2009; Ghazali et al., 2010; Routh et al., 2011; Choi and Alkhalifah, 2012; Guitton and Diaz, 2012;

Manuscript received by the Editor 28 April 2014; revised manuscript received 26 December 2014; published online 27 April 2015.
[1]Delft University of Technology, Department of Imaging Physics, Delft, Zuid Holland, Netherlands. E-mail: a.k.soni@tudelft.nl.
[2]Delft University of Technology, Faculty of Applied Sciences, Department of Imaging Science and Technology, Delft, Netherlands. E-mail: d.j.verschuur@tudelft.nl.

Plessix et al., 2012) of the blended seismic data directly, without actively separating the sources in advance.

Along this latter approach, we propose full-wavefield migration (FWM) to image blended VSP data. For theoretical details on FWM and its application to surface seismic data, see, for example, Berkhout (2012, 2014b) Davydenko et al. (2012), and Davydenko and Verschuur (2013, 2014). The application of FWM to image unblended VSP data is discussed in Soni et al. (2012) and Soni and Verschuur (2013a, 2013c, 2014a), and initial reports on imaging blended VSP data are discussed in Soni and Verschuur (2013b, 2014b). We know that imaging the blended shot records directly causes crosstalk noise in the image due to wavefield interference. Hence, an inversion-based imaging scheme is better suited to reduce such noises compared to correlation-based imaging (Verschuur and Berkhout, 2011). FWM is an inversion-based imaging algorithm to estimate the subsurface reflectivity using the primaries as well as all the multiples (surface and internal multiples) in the recorded wavefield. The multiple scattering enhances the illumination as well as the resolution of the image. The least-squares inversion scheme can handle the incoherent blended source data more effectively than a correlation-based imaging scheme and helps to suppress the extrapolation artifacts and blending crosstalk. In the following sections, we will discuss full-wavefield modeling and FWM for blended VSP experiments. We will illustrate the potential of FWM in imaging blended VSP data using numerical examples.

FULL-WAVEFIELD MODELING FOR A BLENDED VERTICAL SEISMIC PROFILING GEOMETRY

Theory

The full-wavefield modeling algorithm (Berkhout and Verschuur, 2011; Berkhout, 2012, 2014a; Davydenko et al., 2012; Soni et al., 2012; Soni and Verschuur, 2014a) is based on the integral solution of the wave equation. Full-wavefield modeling uses the subsurface reflectivity as a modeling parameter instead of the medium elastic parameters that are required in finite-difference methods. This modeling scheme is recursive in depth and iterative, where each iteration adds a higher order of multiple scattering at all depth levels. Note that in the modeling, we assume a scale separation between the background or migration velocity and the reflectivity operators, which independently governs the wavefield propagation and the amplitude of the wavefield, respectively. On the other hand, in finite-difference schemes, the propagation effects and scattering effects are coupled. Furthermore, in full-wavefield modeling, the inhomogeneities in the migration velocity model do not create multiples in the modeling: The multiples are generated by the reflectivities only. In full-wavefield modeling, the wavefield relationships at a discontinuity are similar to those of the reflectivity method (Claerbout, 1976; Kennett, 1979).

As described in Soni et al. (2012) and Soni and Verschuur (2013a, 2014a), we define a modeling scheme for a VSP acquisition geometry in the reciprocal domain, which means that the receivers are considered to be located at the surface, whereas the sources are located in a borehole. In other words, the data are modeled in the common-receiver domain. However, in a blended-source field experiment, blending of sources is performed at the surface. Therefore, we can say that the source-side blending in the original field experiment is equivalent to a receiver-side blending in the reciprocal domain, using the transposed blending operator (for details on receiver-side blending, see Berkhout et al., 2009).

In data matrix notations (for one frequency component), $\mathbf{P}_{\mathrm{vsp}}$ and $\mathbf{P}_{\mathrm{vsp,bl}}$ represent unblended and blended VSP data, respectively. A column-vector and a row-vector of these matrices represent a common-source gather and a common-receiver gather, respectively. In the reciprocal domain, the data matrices are represented by $\mathbf{P}^T_{\mathrm{vsp}}$ and $\mathbf{P}^T_{\mathrm{vsp,bl}}$ (transpose of the original matrices), where a column-vector and a row-vector of the matrices now represent a common-receiver gather and a common-source gather, respectively. Furthermore, in terms of matrix multiplications, a blending operator Γ_{bl} applied on the right side of the data matrix $\mathbf{P}_{\mathrm{vsp}}$ is equivalent to source-side blending. However in the reciprocal domain, the transposed blending operator Γ^T_{bl} applied on the left side of the reciprocal domain data matrix $\mathbf{P}^T_{\mathrm{vsp}}$ indicates receiver-side blending (Soni and Verschuur, 2014b). Figure 1 schematically illustrates this relationship.

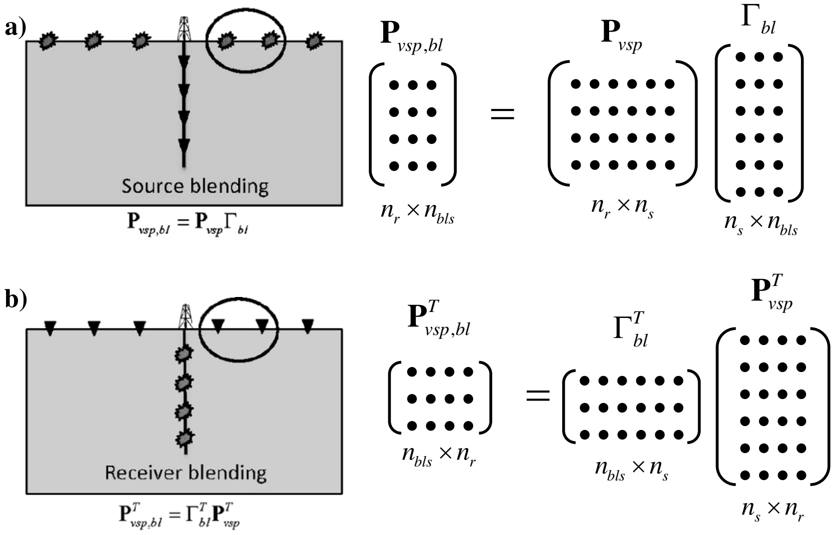

Figure 1. Schematic diagram showing the equivalence of (a) source-side blending $\mathbf{P}_{\mathrm{vsp}}\Gamma_{\mathrm{bl}}$, for original surface-source walkaway VSP data with (b) receiver-side blending $\Gamma^T_{\mathrm{bl}}\mathbf{P}^T_{\mathrm{vsp}}$, for walkaway VSP data in the reciprocal domain. The matrix multiplication is depicted schematically, where n_s denotes the number of unblended surface sources, n_r denotes the number of borehole receivers, and n_{bls} denotes the number of blended surface sources for the original experiment. The circled shots in (a) and receivers in (b) schematically represent a blending factor of two.

Now, any column vector of the blending operator Γ_{bl} can be written as (Berkhout, 2008)

$$\vec{\Gamma}_{\mathrm{bl}}(z_0) = [\gamma_1, \gamma_2, \gamma_3, \cdots\cdots, \gamma_{ns}], \tag{1}$$

where the nth element γ_n is given by

$$\gamma_n = a_n e^{-j\omega T_n}. \tag{2}$$

In this case, T_n is a random time shift applied to individual sources, a_n is a scale factor that can be zero for those sources not included in the blended experiment, and ns is the number of sources in an unblended experiment (Figure 1). Note that z_0

represents the surface level and $\vec{\Gamma}_{\mathrm{bl}}(z_0)$ represents the blending process being performed at the surface. We will use the term *blending factor* (N_{bl}) to define the number of shots added together to make one blended source experiment. In other words, the blending factor in this paper is defined as the ratio between the number of sources in the unblended survey and the number of blended records in the blended survey. We will illustrate examples of the blending operators with different blending factors in the next section on numerical examples.

Now let us discuss the forward modeling of unblended VSP data in the common-receiver domain. Mathematically, the down- and upgoing wavefields incident at a depth level z_n from above and from below, respectively, can be written as (Soni and Verschuur, 2014a)

$$\begin{aligned}\vec{Q}^{+}(z_n) &= \vec{P}^{+}(z_n) + [\mathbf{R}^{\cup}(z_n)\vec{P}^{+}(z_n) \\ &\quad + \mathbf{R}^{\cap}(z_n)\vec{P}^{-}(z_n)] \\ &= \vec{P}^{+}(z_n) + \delta\vec{P}(z_n)\end{aligned} \tag{3}$$

and

$$\begin{aligned}\vec{Q}^{-}(z_n) &= \vec{P}^{-}(z_n) + [\mathbf{R}^{\cup}(z_n)\vec{P}^{+}(z_n) \\ &\quad + \mathbf{R}^{\cap}(z_n)\vec{P}^{-}(z_n)] \\ &= \vec{P}^{-}(z_n) + \delta\vec{P}(z_n),\end{aligned} \tag{4}$$

where $\vec{Q}^{-}(z_n)$ and $\vec{P}^{+}(z_n)$ represent the up- and downgoing wavefields just above depth level z_n, respectively, and $\vec{Q}^{+}(z_n)$ and $\vec{P}^{-}(z_n)$ represent the down- and upgoing wavefields just below depth level z_n, respectively. Figure 2 illustrates this wavefield convention. The $+$ and $-$ superscript signs represent the downgoing and upgoing directions, respectively. The matrices $\mathbf{R}^{\cup}(z_n)$ and $\mathbf{R}^{\cap}(z_n)$ represent reflectivity matrices related to the discontinuities at depth level z_n for the wavefield coming from above and from below the layer, respectively. The diagonal of the reflectivity matrices contains the zero-offset reflection coefficients, and the angle-dependent reflectivity information is contained in the full reflectivity matrices (see also de Bruin et al., 1990). Note that in the case of imaging angle-independent reflectivity, the $\mathbf{R}$-matrices are diagonal matrices that are frequency independent. For the case of including angle dependency, the matrices become frequency dependent, in a controlled manner, because the angle-dependent reflection information is located at zero intercept time in the linear Radon domain. Therefore, constraints should be put on $\mathbf{R}$ when estimating angle-dependent reflectivity (Berkhout, 2014b). For the examples in this paper, all images are created under the angle-independent reflectivity assumption. Figure 3 schematically illustrates the structure of the $\mathbf{R}$ matrix and shows an example of the angle-dependent and angle-independent reflectivity vector in the space-time domain at a grid point located on a reflector. Note that in this paper, we will restrict ourselves to estimate angle-independent reflectivities only. Furthermore, in this paper, we discuss PP imaging neglecting converted waves.

The two-way scattered wavefield $\delta\vec{P}(z_n)$ can be written as

$$\delta\vec{P}(z_n) = [\,\mathbf{R}^{\cup}(z_n) \quad \mathbf{R}^{\cap}(z_n)\,]\begin{bmatrix}\vec{P}^{+}(z_n)\\ \vec{P}^{-}(z_n)\end{bmatrix} = \mathbf{R}(z_n)\vec{P}(z_n), \tag{5}$$

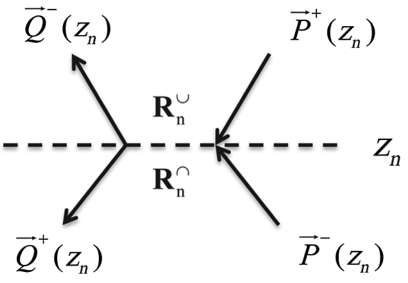

Figure 2. Schematic diagram showing the up- and downgoing wavefields at depth level z_n. The up- and downgoing wavefields just above depth level z_n are represented by $\vec{Q}^{-}(z_n)$ and $\vec{P}^{+}(z_n)$, respectively, and the ones just below depth level z_n are represented by $\vec{P}^{-}(z_n)$ and $\vec{Q}^{+}(z_n)$, respectively. The matrices $\mathbf{R}^{\cup}(z_n)$ and $\mathbf{R}^{\cap}(z_n)$ represent reflectivity matrices related to the discontinuities at depth level z_n for the wavefield coming from above and below the level, respectively.

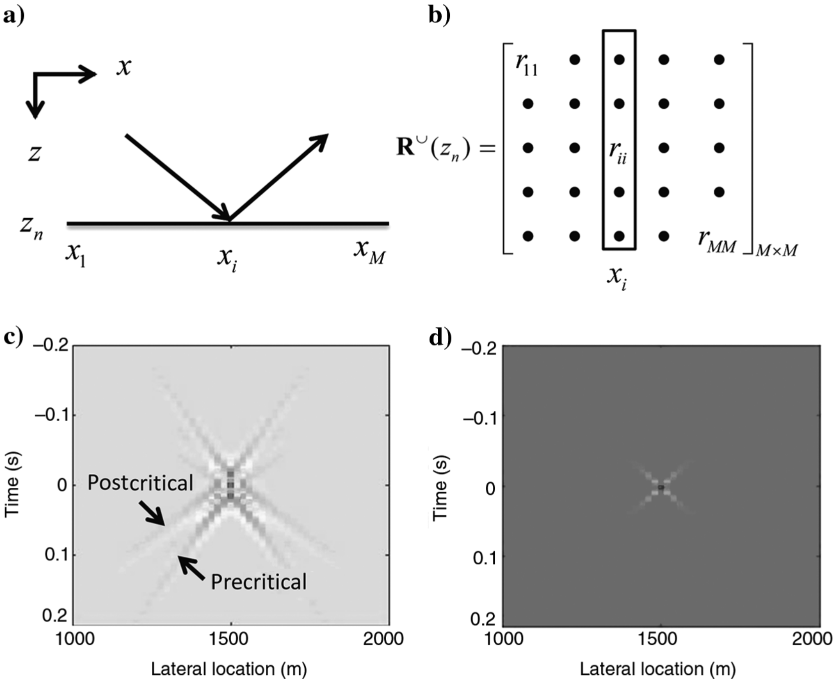

Figure 3. Description of reflectivity matrix $\mathbf{R}$. Matrix $\mathbf{R}^{\cup}(z_n)$ represents reflectivity for (a) an arbitrary depth level z_n for all lateral locations x_1 to x_M in a gridded model. (b) The reflectivity matrix $\mathbf{R}$ for one frequency component, in which one column vector at grid point location x_i represents the corresponding angle-dependent reflectivity. The reflectivity vector of the grid point x_i is shown in the space-time domain for (c) angle-dependent and (d) angle-independent reflection. Note the complex angle-dependent reflectivity behavior computed for a high-velocity contrast, horizontally layered medium in panel (c), showing the precritical and postcritical reflections. On the other hand, panel (d) shows the angle-independent reflectivity, which is a scalar value for one grid-point location (shown by a band-limited spike), i.e., when the reflectivity matrix R is a diagonal matrix.

where $\mathbf{R}$ is the total reflectivity matrix and $\vec{P}(z_n)$ is the total incident wavefield, for a depth level z_n, from above and below. For a small S-wave velocity contrast and for precritical angles, $\mathbf{R}^{\cap}(z_n) = -\mathbf{R}^{\cup}(z_n)$. In equations 11 and 4, the terms $\vec{P}^+(z_n) + \mathbf{R}^{\cup}(z_n)\vec{P}^+(z_n) = \mathbf{T}^+(z_n)\vec{P}^+(z_n)$ and $\vec{P}^-(z_n) + \mathbf{R}^{\cap}(z_n)\,\vec{P}^-(z_n) = \mathbf{T}^-(z_n)\vec{P}^-(z_n)$ can be recognized as the transmitted down- and upgoing wavefields through depth level z_n. $\mathbf{T}^+(z_n)$ and $\mathbf{T}^-(z_n)$ represent the transmissivity matrices for depth level z_n.

Furthermore, the one-way wavefield propagation for downgoing and upgoing wavefields from one depth level to other, respectively, can be written as

$$\vec{P}^+(z_n) = \mathbf{W}^+(z_n, z_{n-1})\vec{Q}^+(z_{n-1}) \tag{6}$$

and

$$\vec{P}^-(z_n) = \mathbf{W}^-(z_n, z_{n+1})\vec{Q}^-(z_{n+1}), \tag{7}$$

where $\mathbf{W}^+(z_n, z_{n-1})$ and $\mathbf{W}^-(z_n, z_{n+1})$ are the downward and upward propagation operators. The propagation operators can be calculated in inhomogeneous migration velocity models using a phase-shift and space-frequency convolution operators (Thorbecke et al., 2004).

Now, the iterative full-wavefield modeling can be formulated in terms of iterative modeling of total incident wavefields $\vec{P}(z_n)$ recursively along all depth levels. Mathematically, the incident wavefield from above, i.e., $\vec{P}^+(z_n)$, and from below, i.e., $\vec{P}^-(z_n)$, for a given iteration i can be written as

$$\vec{P}^+(z_n)^{(i)} = \sum_{m=0}^{n-1} \mathbf{W}^+(z_n, z_m)[\delta\vec{P}(z_m)^{(i-1)} + \vec{S}^+(z_m)] \tag{8}$$

and

$$\vec{P}^-(z_n)^{(i)} = \sum_{m=n+1}^{N} \mathbf{W}^-(z_n, z_m)[\delta\vec{P}(z_m)^{(i-1)} + \vec{S}^-(z_m)], \tag{9}$$

where $\vec{S}^+$ and $\vec{S}^-$ are the down- and upgoing sources wavefields, respectively, which are nonzero when there is an active source at that depth level. Note that the first iteration models the direct source wavefields only. In subsequent iterations, $\delta\vec{P}(z_n)$ includes the $\vec{P}^+(z_n)$ and $\vec{P}^-(z_n)$ from the previous iteration. Thus, each iteration leads to one full round trip of the wavefield; i.e., it adds one higher order of scattering. In other words, for a given iteration i, in $\delta\vec{P}(z_n) = \mathbf{R}^{\cup}(z_n)\vec{P}^+(z_n) + \mathbf{R}^{\cap}(z_n)\vec{P}^-(z_n)$, the $\vec{P}^+(z_n)$ and $\vec{P}^-(z_n)$ terms are computed from the previous iteration $(i-1)$. For the scope of this paper, we will consider only the up- and downgoing wavefields, in which the far angles of propagation could be limited by the up- and downgoing extrapolation operators, respectively. However, this concept can be extended to include nearly horizontally traveling wavefields such as turning waves to image very steep or vertical structures. For examples for surface seismic data, see Davydenko and Verschuur (2013, 2014) and for VSP data, see Soni et al. (2014).

Now, in the reciprocal domain, the modeled VSP data $\mathbf{P}^T_{\text{vsp}}$ at any iteration provide the upgoing wavefields at the surface, given by equation 9 for $z_n = z_0$, which is the data due to an unblended shot experiment. Hence, as mentioned earlier, to model the data for a blended VSP source experiment, we perform receiver-side blending to this modeled data in the reciprocal domain, which can be written as

$$\mathbf{P}^T_{\text{vsp,bl}} = \Gamma^T_{\text{bl}}\mathbf{P}^T_{\text{vsp}}. \tag{10}$$

In the next subsection, we will illustrate the full-wavefield modeling of blended VSP data using numerical examples.

Numerical example 1: 2D dipping reflector model

n this section, we will illustrate full-wavefield modeling for blended VSP data using a 2D dipping-layer velocity model and an effective vertical angle-independent (scalar) reflectivity model as shown in Figure 4. For the conventional (unblended) acquisition geometry, the sources are located at the surface between 0 and 3000 m, every 20 m; i.e., we have 151 shots for an unblended geometry.

In the numerical blending, we design the operator such that it applies a random time shift to all the conventional sources at the surface and then add the regularly sampled sources in space at a distance separated by Δx_{bls} to yield the blended survey, where Δx_{bls} is given by

$$\Delta x_{\text{bls}} = \frac{n_s}{N_{\text{bl}}} \times \Delta x. \tag{11}$$

The maximum randomized time shifts allowed in the blending process do not exceed ±0.1 s. Figure 5 shows an example of the blending operator for blending factors of two, three, and four. The resulting number of shots for blending factors two, three, and four are 76, 51, and 38, respectively.

The receivers are located in the borehole, between a depth of 100 and 1100 m, every 10 m. We illustrate an example of a common-shot gather, which is represented by a column vector of the matrix

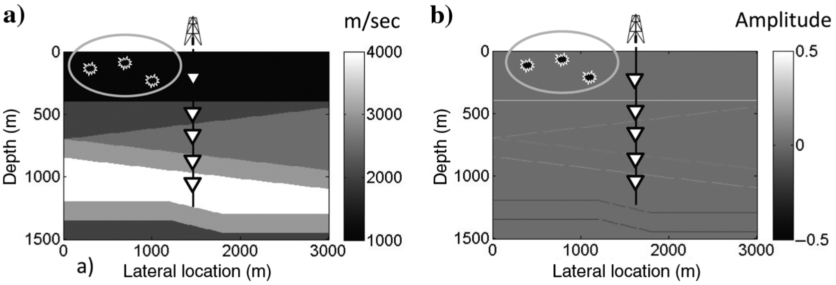

Figure 4. (a) The 2D velocity model and (b) an effective scalar (angle-independent) reflectivity model, annotated with the walkaway blended VSP acquisition geometry, used to illustrate full-wavefield modeling and the inversion scheme. The sources are located at the surface, and the receivers are located at the borehole. Note that the varying depths of the sources as shown schematically in these figures are only to indicate that they are fired at different times. For this example, a constant density is assumed to compute the effective reflectivity model.

$\mathbf{P}_{\mathrm{vsp}}$ for unblended data or a column vector of the matrix $\mathbf{P}_{\mathrm{vsp,bl}}$ for blended data. Further, we also illustrate an example of a common-receiver gather, which is represented by a row vector of the matrix $\mathbf{P}_{\mathrm{vsp}}$ for unblended data or a row vector of the matrix $\mathbf{P}_{\mathrm{vsp,bl}}$ for blended data. Figures 6 and 7 show the example gathers for iterations one, two, and three as well as for blending factors of one, two, three, and four, respectively. Note that in Figure 6, each iteration adds a higher order of multiples: For a given blended source experiment and with increasing blending factors, the wavefields become more and more complex due to wavefield interferences. Furthermore, note that in Figure 7, the common-receiver domain shows random events for blending factors higher than one and shows that the number of traces (which is equal to the number of blended experiments) decreases as the blending factor increases. In the next section, we will discuss the least-squares inversion scheme in FWM.

FWM OF BLENDED VERTICAL-SEISMIC-PROFILING DATA IN THE COMMON-RECEIVER DOMAIN

Theory

In this section, we discuss the FWM process that aims at estimating the true-amplitude reflectivity image directly from the blended VSP data. The imaging is posed as a least-squares inversion scheme (for details, see also Soni and Verschuur, 2014a, 2014b). Figure 8 shows a generalized block diagram for the inversion scheme in FWM to image blended VSP data in the common-receiver domain. Note that the intermediate pseudodeblended residual is imaged, yielding a subsurface reflectivity that is used in full-wavefield modeling (in the reciprocal domain), which is subsequently blended by the same blending operator used in the data acquisition. The estimated blended data are then compared with the measured blended data. The residual of the measured and simulated data are minimized in a least-squares sense to update the reflectivity iteratively. Note that in FWM, each iteration adds and uses a higher order of multiples. Because the migration is performed as a feedback process, the first iteration is similar to conventional imaging of the primary wavefields. Next, each iteration of FWM involves an iteration of full-wavefield modeling and hence, adds or uses a higher order of multiples to estimate the reflectivity. With subsequent iterations of FWM, the image becomes more accurate and sharper; i.e., the vertical resolution increases, and the full wavefield is better explained. This is the same as in other least-squares imaging schemes: With subsequent iterations, the estimated reflectivity converges to a reasonable solution. However, in addition, each new iteration in FWM explains higher order scattering effects in the data. Therefore, it is interesting to note that if we replace the nonlinear full-wavefield modeling with a linear Born-modeling operator, which models only the upgoing primary wavefield, the block diagram is equivalent to what we call *least-squares migration* (Nemeth et al., 1999).

Pseudodeblending is the generalized inverse of the blending matrix (see also Berkhout, 2008; Mahdad, 2012; Doulgeris, 2013). Mathematically, if the blended VSP data matrix for one frequency component is written as $\mathbf{P}_{\mathrm{vsp,bl}} = \mathbf{P}_{\mathrm{vsp}}\Gamma_{\mathrm{bl}}$, then we can estimate the pseudodeblended VSP data $\mathbf{P}_{\mathrm{vsp,pdbl}}$ by finding the least-squares solution of the equation above as

$$\mathbf{P}_{\mathrm{vsp,pdbl}} = \mathbf{P}_{\mathrm{vsp,bl}}[\Gamma_{\mathrm{bl}}^{H}\Gamma_{\mathrm{bl}}]^{-1}\Gamma_{\mathrm{bl}}^{H}. \tag{12}$$

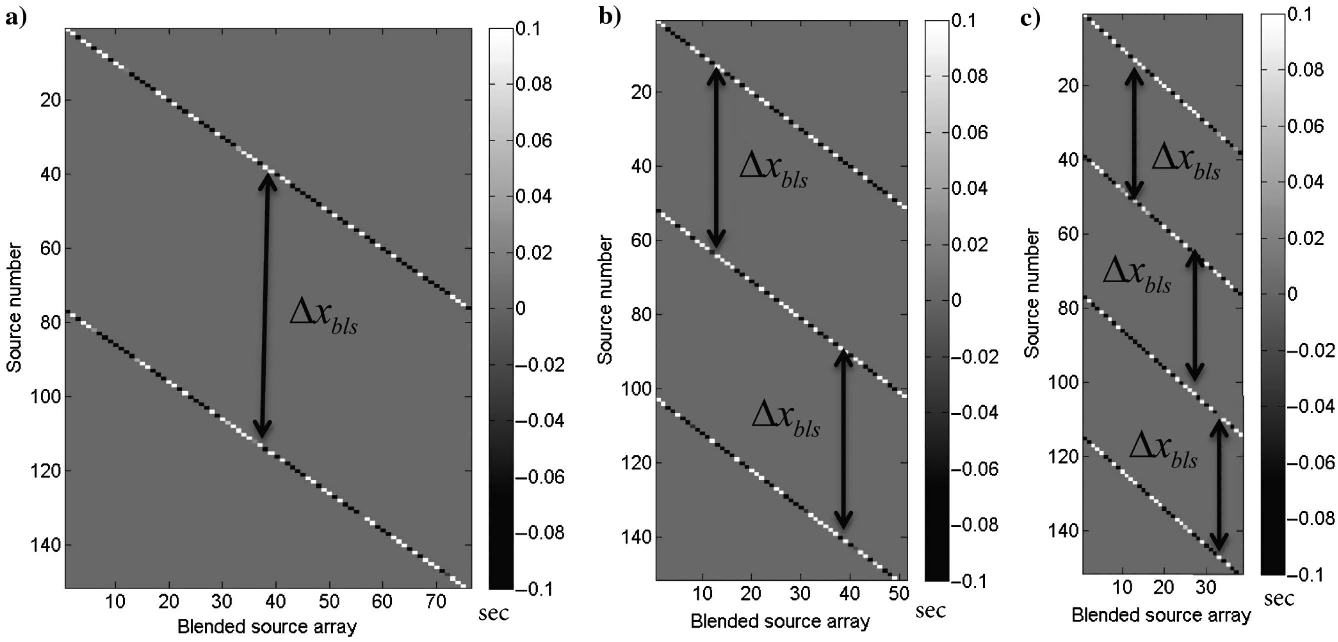

Figure 5. An example of the blending operator depicting a random time shift that is applied to a regularly separated sources in space (separated by a distance of Δx_{bls}) and then summed to obtain blended source arrays, for blending factors of (a) two, (b) three, and (c) four. In these figures, the colors of the elements of the matrices represent the time shift applied to different sources in the blending process, which is between −0.1 and 0.1 s. Also note that Δx_{bls} only shows the lateral distance between the sources in a schematic way and does not comply with the axes of these figures, which indicate the source numbers.

The subscripts "bl" and "pdbl" refer to the blended and pseudodeblended VSP data. The superscript H represents the Hermitian of a matrix or vector. For our numerical examples, the matrix $[\Gamma_{\mathrm{bl}}^{H}\Gamma_{\mathrm{bl}}]^{-1} = 1/b\,\mathbf{I}$, where b is the number of blended sources. So equation 13 is reduced to

$$\mathbf{P}_{\mathrm{vsp,pdbl}} = \frac{1}{b}\mathbf{P}_{\mathrm{vsp,bl}}\Gamma_{\mathrm{bl}}^{H}. \tag{13}$$

In the blended source experiment, data appear blended in the common-shot domain; however, it appears randomized in the common-receiver domain. Therefore, in the case of blended surface seismic data, the blended shot records can directly be used in the least-squares-based migration algorithms (see, for example, Verschuur and Berkhout, 2009, 2011). However, in the case of blended VSP data, to perform common-receiver domain imaging, we need to perform an intermediate pseudodeblending in the algorithm.

FWM for blended VSP data is formulated as a least-squares inversion scheme and can be written as the minimization of the following objective function:

$$J = \sum_{k}\sum_{\omega}\|\vec{P}^{-}_{\mathrm{bl,obs},k} - \vec{P}^{-}_{\mathrm{bl,est},k}\|_2^2, \tag{14}$$

where $\vec{P}_{\mathrm{bl,obs}}$ and $\vec{P}_{\mathrm{bl,est}}$ are the observed and the estimated blended VSP data. The subscript k is for the kth blended source experiment. The above optimization problem can be solved by an iterative conjugate gradient scheme (Hestenes and Stiefel, 1952) to estimate the reflectivity of the subsurface. Appendix A discusses this inversion scheme in detail. Note that in the iterative minimization scheme, the energy of the total blended data is minimized in the least-squares sense. Furthermore, note that the residual energy of the pseudodeblended data (which is used to compute the gradient) increases with the increasing blending factor, due to an increase in the blending noise. We also observe an increase in noise leakage or blending crosstalk in the image space with increasing blending factors. We will illustrate these aspects later in this paper.

In the next subsection, we illustrate the FWM of blended VSP data using numerical examples.

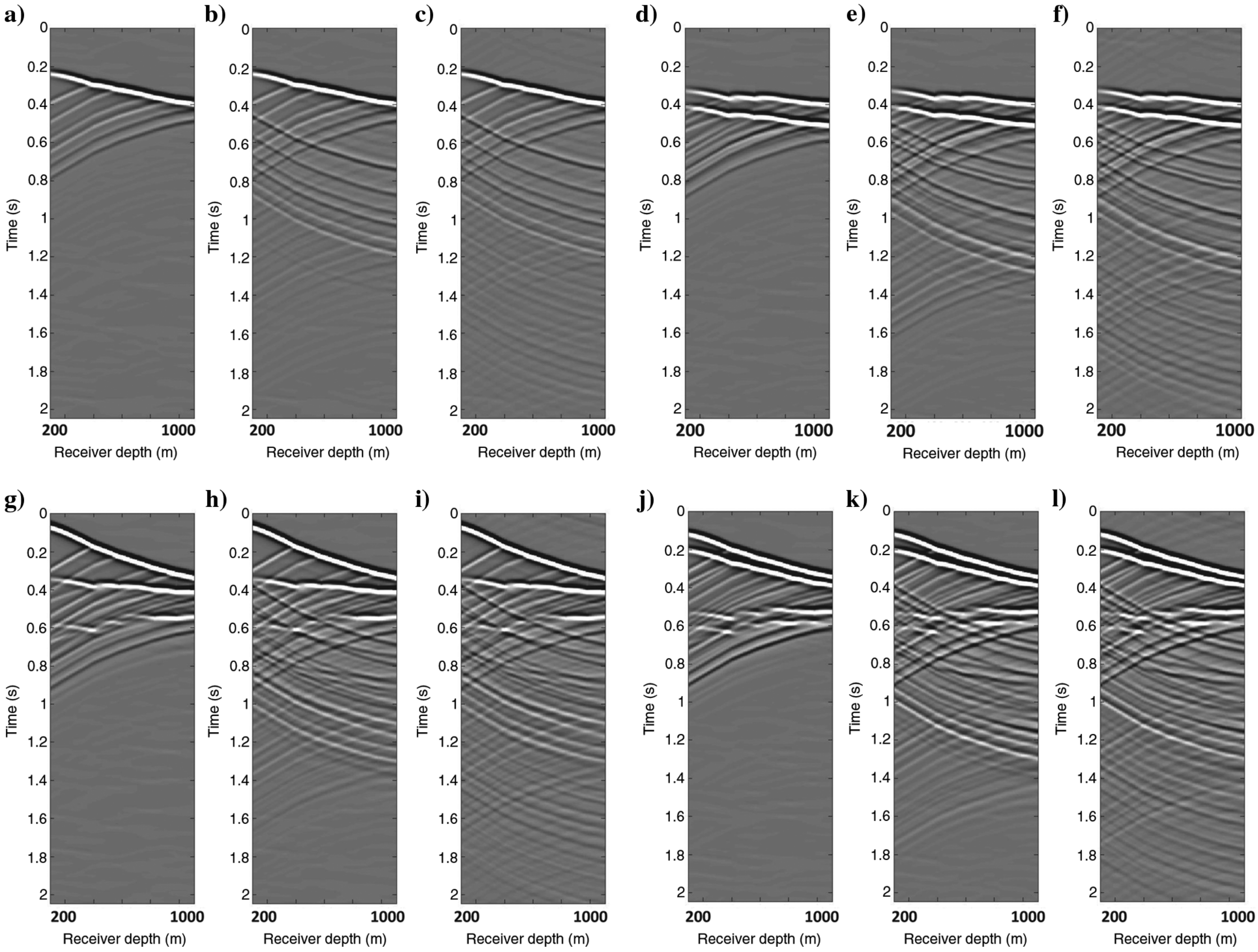

Figure 6. Modeled VSP data for the velocity and reflectivity model shown in Figure 4, using full-wavefield modeling for blended source experiments. Panels (a–c) show an example common-shot gather for blending factor = 1 (unblended), after the first, second, and third iterations, respectively. Panels (d, f, g, i, j, and l) show a similar example for blending factors of two, three, and four, respectively.

Numerical example 1: 2D dipping layer model

To illustrate the inversion scheme, we have modeled unblended VSP data using an acoustic 2D finite-difference method, using a dipping-layer velocity model shown in Figure 4a and a constant density. The unblended VSP data are simulated for uniformly distributed sources, laterally located between 0 and 3000 m, with a source spacing of 20 m at the surface. The receivers are located between a depth of 100 and 1100 m, every 10 m. The simulated unblended VSP data are then numerically blended by adding shots with random time shifts. We will illustrate the FWM scheme for blending factors of one, two, three, and four.

Figure 9 shows the images obtained after the first and tenth iterations, using the blended data with blending factors of one, two, three, and four. Note that the image after the first iteration is equivalent to the image obtained using primary-only wavefields via any conventional migration technique. Also, with the increasing blending factors, the blending crosstalk noise due to wavefield interference increases: This is observed both primary only in Figure 9a, 9c, 9e, and 9g (after the first iteration) and for full-wavefield images in

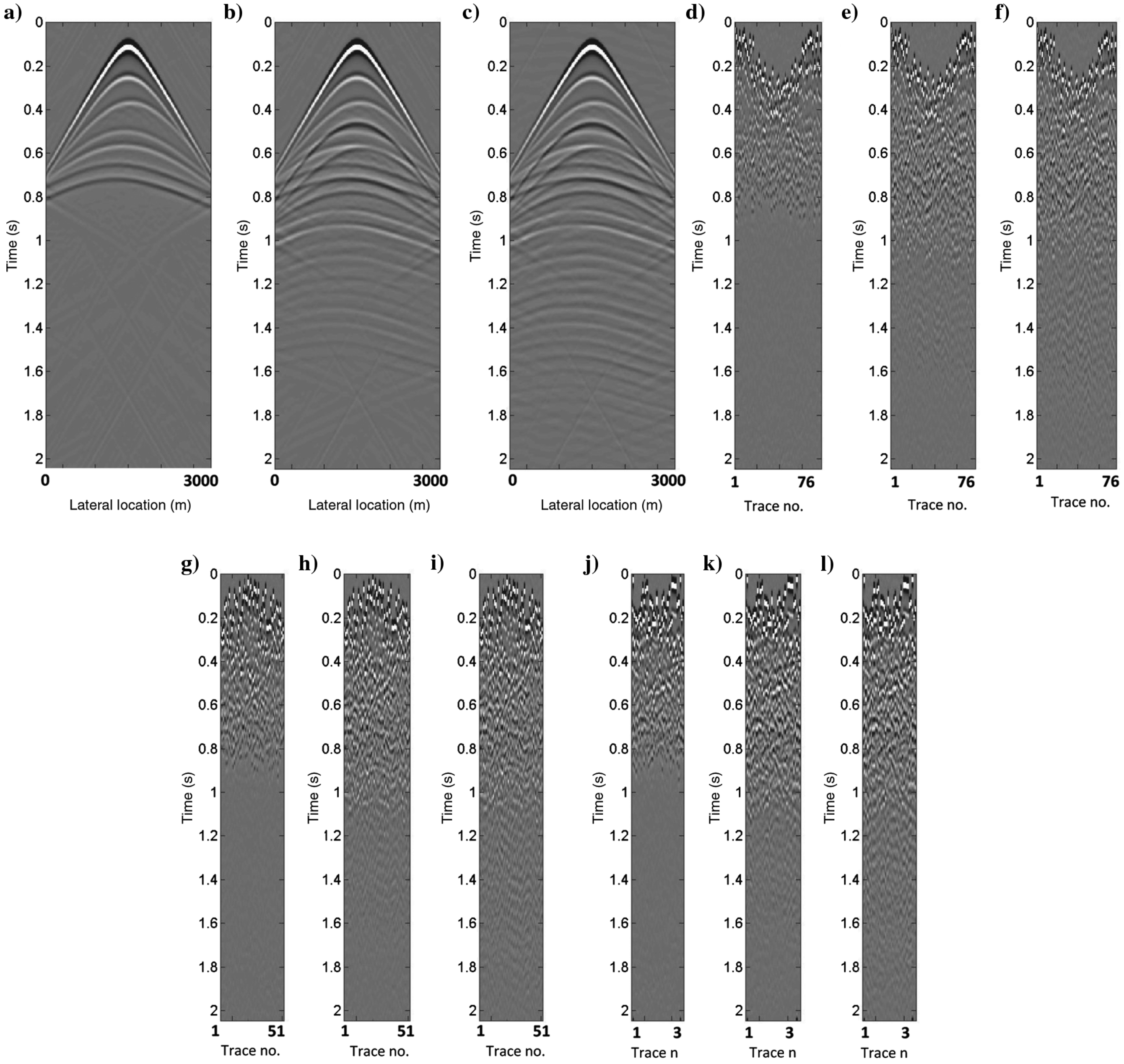

Figure 7. Modeled VSP data for the velocity and reflectivity model shown in Figure 4, using full-wavefield modeling for blended source experiments. Panels (a–c) show an example common-receiver gather for blending factor = 1 (unblended), after the first, second, and third iterations, respectively. Panels (d, f, g, i, j, and l) show a similar example for blending factors of two, three, and four, respectively. Note that with the increase in the blending factor, the number of traces in the common-receiver domain decreases.

Figure 9b, 9d, 9f, and 9h (after the tenth iteration). However, inversion-based FWM helps suppress the crosstalk noise to provide a reasonable image even for blended data with higher blending factors. Also, the multiples iteratively enhance the illumination as well as the vertical resolution of the images in FWM. Of course, there is a trade-off between the noisy image obtained and the acquisition cost involved: For example, a blending factor of four makes the acquisition cost one-fourth of the original (assuming that cost linearly increases with acquisition time). Also note that due to inaccurate source wavefield estimation, we see some footprints of the

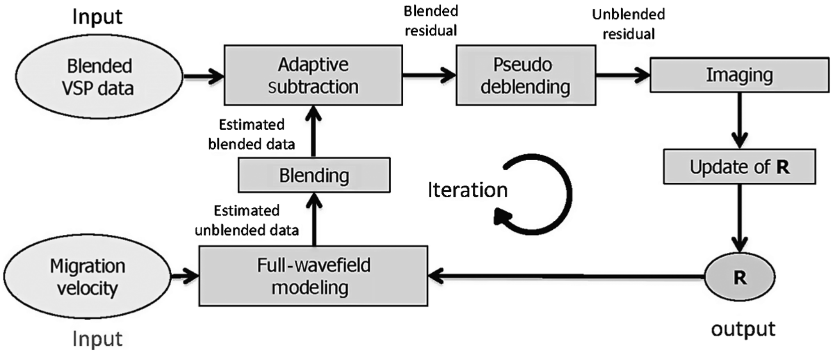

Figure 8. Block diagram: FWM for blended VSP data, showing the feedback loop for the inversion in the common-receiver domain. The intermediate pseudodeblended data are imaged, yielding a subsurface reflectivity that is used to simulate the response using full-wavefield modeling (in the reciprocal domain), and then they are blended by the same blending operator used in data acquisition. The blended estimated data are compared with the measured blended data. The residual of the measured and simulated data after adaptive subtraction is fed back into the loop to iteratively update the reflectivity. Each iteration adds or uses a higher order of multiples.

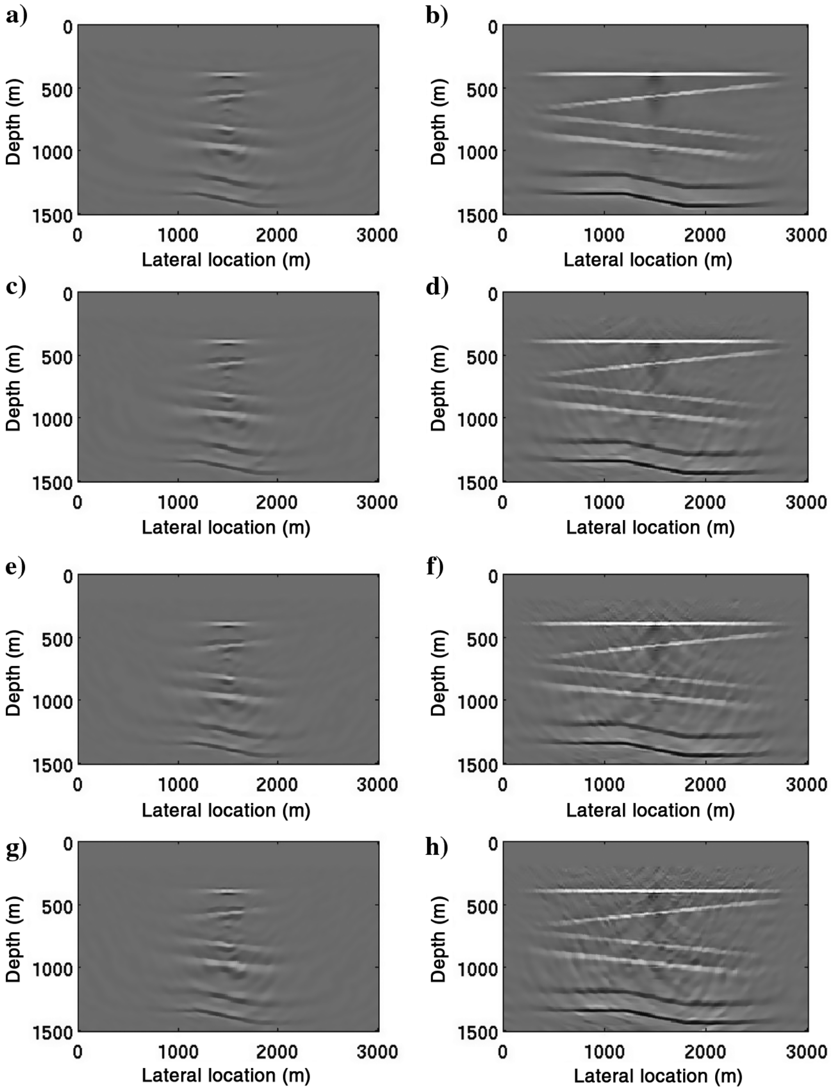

Figure 9. The 2D dipping-layer model: image comparison after the first and tenth iterations of FWM on blended VSP data with different blending factors. Panels (a, c, e, and g) show the image after the first iteration of FWM using blended VSP data with blending factors of one, two, three, and four, respectively; and panels (b, d, f, and h) show the image after the tenth iteration of FWM using blended VSP data with blending factors of one, two, three, and four, respectively.

receivers as a near-field effect. These footprints appeared to be less in higher blending factors, just because they are overshadowed by the blending interference noise in the image.

Furthermore, Figure 10 compares the observed and estimated blended data after the tenth iteration of FWM for different blending factors using a common-shot gather. Hence, we see from the data misfit that FWM explains the full wavefield for the blended source experiment while estimating subsurface reflectivity. However, we also see that the data misfit is relatively larger for higher blending factors. Figure 11 shows the convergence curves for the normalized objective function as well as the normalized energy of the pseudo-deblended residual (which is used to compute the gradient) with respect to the number of iterations of FWM for blended VSP data. Note again that the convergence rate is slower for data with a higher blending factor, as shown in Figure 11a. Furthermore, in these examples, the convergence of the algorithm becomes slow beyond the tenth iteration. So, we set this maximum number of iterations as a stopping criterion for these tests. Furthermore, Figure 11b clearly indicates the increase in the fraction of blending noise in the data with the increasing blending factor.

As an additional experiment, we select every fourth shot from the unblended VSP data (i.e., a total of 38 shots of 151 shots), equally spaced at the surface. The size of these data is equivalent to data with a blending factor of four. These decimated data were migrated using FWM. Figure 12c shows the image obtained after the tenth iteration. We can compare this image with the image obtained using VSP data with a blending factor of four, as shown in Figure 12a (same as Figure 9h). Note that when using FWM, the multiples do help to give a reasonable image even using a sparse survey data. However, we can observe aliasing noise in the shallow area. In addition, for the decimated data, we can clearly see the correlated reflection energy in the difference plot (Figure 12d), whereas for the blended case, the difference plot (Figure 12b) mainly shows the residual blending crosstalk. We compute the noise percentage in

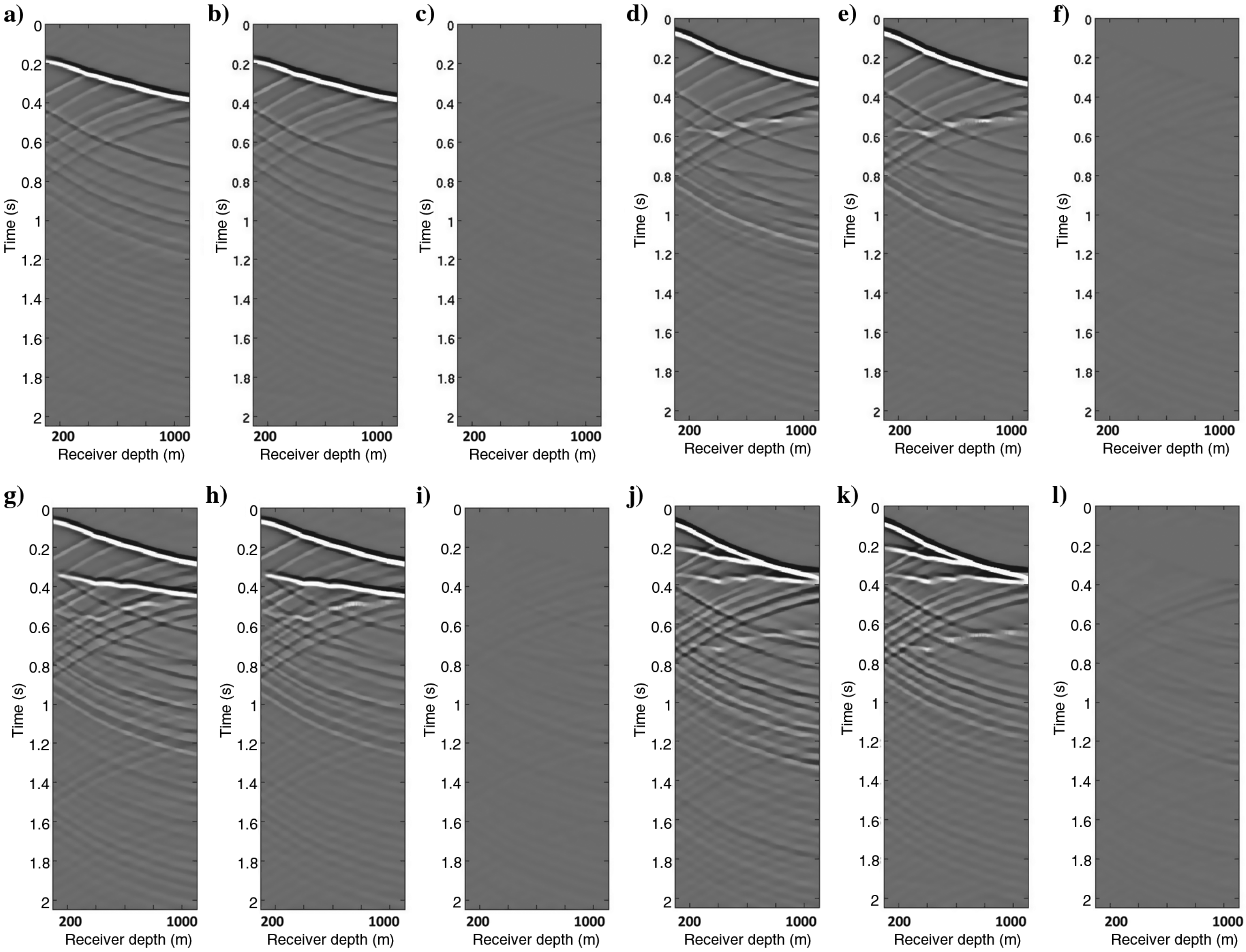

Figure 10. The 2D dipping-layer model: Comparison of observed data, estimated data, and data misfit after the tenth iteration of FWM on the blended VSP data with different blending factors. Panels (a, d, g, and j) show an example observed or measured common-shot gather for blending factors of one, two, three, and four, respectively; panels (b, e, h, and k) show the corresponding estimated common-shot gather for blending factors one, two, three, and four, respectively; and panels (c, f, i, and l) show the corresponding data misfit for blending factors of one, two, three, and four, respectively.

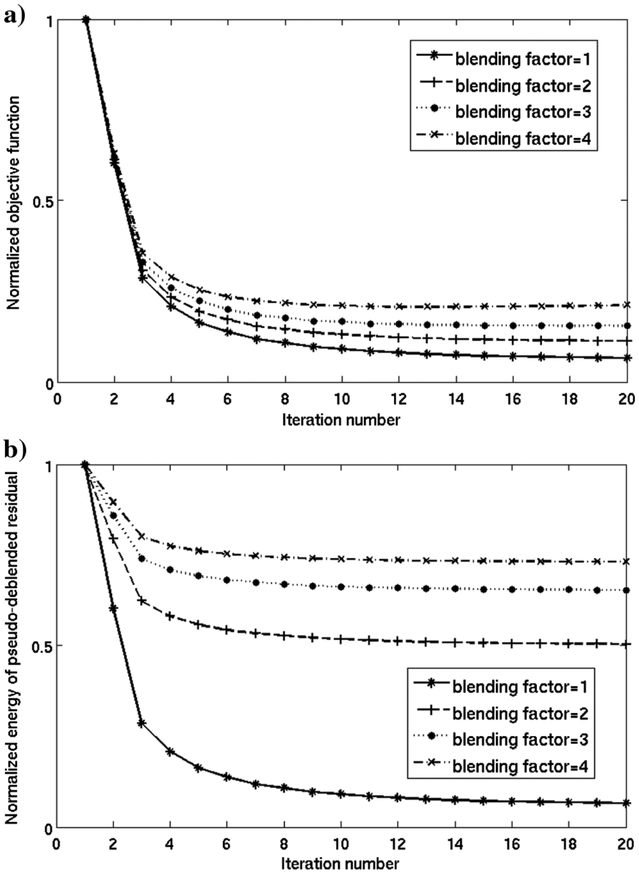

Figure 11. The 2D dipping-layer model: (a) convergence curves depicting the minimization of the normalized objective function with respect to the number of iterations. Note that the convergence rate is slower for data with a higher blending factor. Panel (b) shows the normalized energy of the pseudodeblended residual (which is used to compute the gradient) with respect to the number of iterations. This graph clearly indicates the increase in the fraction of blending noise in the data with the increasing blending factor.

the image obtained using data with a blending factor of four and the image obtained using one-fourth of the unblended data, keeping the image obtained using the dense unblended survey as the reference, all after the tenth iteration of FWM. Quantitatively, the noise percentage in the difference image from a blending factor of four is approximately 5%, whereas the noise percentage in difference image from the decimated data is approximately 12%. The noise here is defined as the ratio of the root-mean-square (rms) value of the difference image amplitudes with respect to the rms value of the image amplitudes obtained using the dense unblended data, expressed as a percentage. The difference image is the difference between the image obtained using the dense unblended data and the image obtained using blended or decimated data.

Next, we will illustrate the effect of a wrong velocity in imaging blended VSP data when used in the FWM algorithm. For the test, we migrate the data using a migration velocity with errors of −5% and +5%. Figure 13 shows the images obtained after the first and tenth iterations, using the blended data with blending factors of one and four. As expected, the images obtained using the wrong migration velocity model are degraded. Note that VSP imaging is more sensitive to a wrong velocity for locations further away from the well because the wavefield travels more for far-offset sources. However, the multiples and primaries behave in a similar way when the wrong velocity model is used in the migration. In addition, the advantage of the inversion-based FWM algorithm is that a wrong velocity model leads to a significantly high residual; i.e., the convergence of the algorithm is very slow. This in fact provides an indication of a wrong velocity model used in the migration. Recently, the concept of joint migration inversion has been introduced, which is an extension of FWM to simultaneously estimate both reflectivity as well as migration velocity. For more details, see Staal and Verschuur (2012, 2013), Staal et al. (2014), and Berkhout (2014c). This concept exploits the fact that a wrong velocity model yields a high residual that could help in a velocity update. A similar concept to estimate migration velocity simultaneously with imaging for VSP data is undergoing ongoing research.

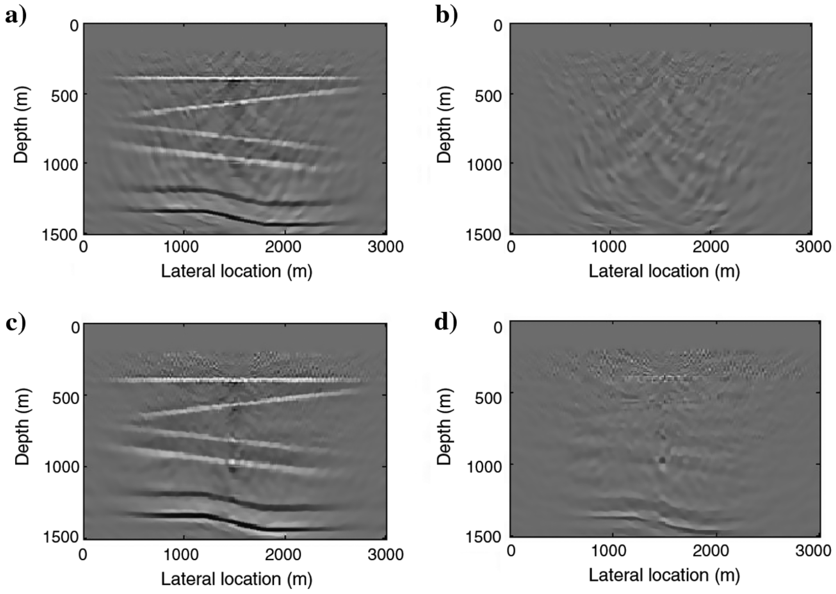

Figure 12. The 2D dipping-layer model: Panel (a) shows the image obtained after the tenth iteration of FWM using the data with a blending factor of 4 (38 blended shots), the same as in Figure 9h and panel (b shows the difference between the image obtained after the tenth iteration of FWM using unblended data (shown by Figure 9b and panel [a]). Panel (c) show the image after the tenth iteration of FWM, using one-fourth of the unblended VSP data (i.e., decimated data, 38 shots), and panel (d) shows the difference between the image obtained after the tenth iteration of FWM using unblended data (shown by Figure 9b and panel [c]).

Numerical example 2: 2D Marmousi model

In this subsection, we illustrate the FWM inversion scheme on a complex Marmousi velocity model (scaled in size) shown in Figure 14. Again, the unblended VSP data were simulated using a 2D acoustic finite-difference method. The unblended VSP data are simulated for uniformly distributed sources at the surface, laterally located between 0 and 3000 m, every 20 m. The receivers are located between a depth of 100 and 1100 m, every 10 m. The simulated unblended VSP data were then numerically blended by adding shots with random time shifts. We have tested the scheme for blending factors of one, two, three, and four. Figure 15 shows the images obtained after the first and twentieth iteration, using the blended data with blending factors of one, two, three, and four, respectively. Similar to the previous examples, we see that the multiples iteratively enhance the illumination as well as the vertical resolution of the images. Again, the crosstalk noise increases with higher blending factors. Note again that due to an inaccurate estimation of the source wavefield, we see some footprints of the receivers as a near-field effect. These footprints appeared to be less in higher blending factors because they are overshadowed by the blending interference noise in the image.

Finally, for this synthetic model, we also show the pseudodeblended residual. Figure 16 compares the pseudodeblended data at the first iteration (i.e., the pseudodeblended measured data), estimated unblended data after the twentieth iteration of FWM and their difference, for different blending factors, using an example common-receiver gather. Note how the imaging process helps to separate out the blending noise as shown in the difference plots in Figure 16. Clearly, we see higher blending noise with the increasing blending factor in the observed data. We also observe that in an unconstrained least-squares minimization process, some of this blending noise can leak into the image space obtained in FWM. As an overall conclusion on this example, we see that the FWM algorithm is capable of handling more complicated data sets.

DISCUSSION

In this paper, we have proposed FWM to directly image blended VSP data (without doing an active deblending), in which all multiples can be used effectively to estimate the subsurface reflectivity with an improved resolution and illumination. The main purpose of this paper is to demonstrate the potential of inversion-based FWM to handle blended VSP data and using the complex incoherent full wavefield in VSP imaging without the need of an additional deblending algorithm. In this paper, we restrict ourselves to obtain a structural image or angle-independent reflectivity image. Hence, in this current formulation, the algorithm does not handle sharp lat-

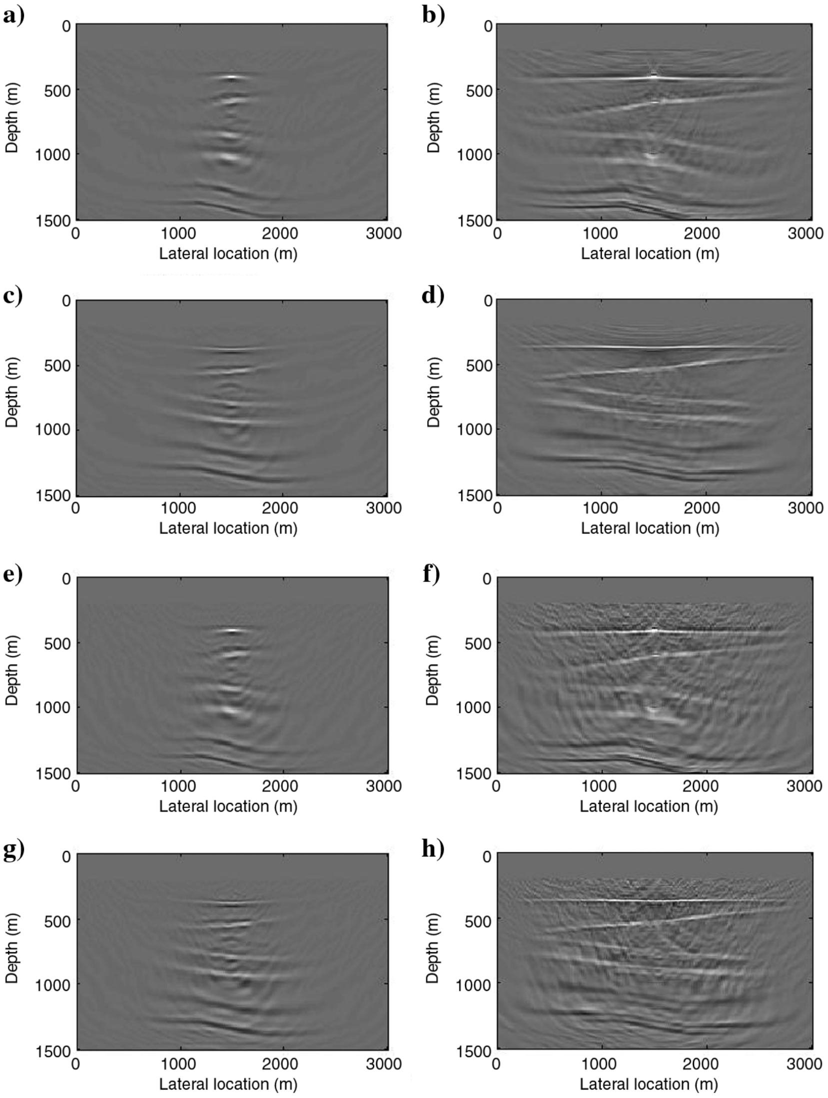

Figure 13. The 2D dipping-layer model: Panels (a and c) show the image after the first iteration of FWM using unblended VSP data and a migration velocity with an error of −5% and +5%, respectively. Panels (b and d) show the corresponding image after the tenth iteration, respectively. Similarly, panels (e and g) show the image after the first iteration of FWM using blended VSP data with a blending factor of four and a migration velocity with an error of −5% and +5%, respectively. Panels (f and h) show the corresponding image after the tenth iteration, respectively.

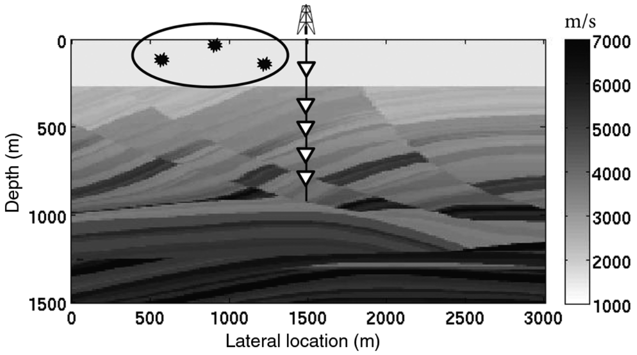

Figure 14. Modified 2D Marmousi velocity model used to model the blended VSP data for imaging.

eral high-velocity contrasts very effectively. The structural image obtained using VSP data represents an effective vertical incidence reflectivity. As mentioned earlier, the method can be extended to include duplex waves and turning waves to image nearly vertical structures.

With FWM, we observe in the image an increased leakage of crosstalk noise with increasing blending factors. Possible solutions to suppress the remaining crosstalk in the image go beyond the scope of this paper. Some of the suggestions include using a regularization term promoting sparsity. Another option could be using a preconditioning to suppress random noise in the pseudodeblended residual before gradient computation. Also, we could use image-based processing by prediction of the blending crosstalk and adaptive subtraction from the obtained image. These aspects are subjects for future research.

The estimation of the source wavefield is highly dependent on how well we can pick the direct arrivals in the measured VSP data. However, picking direct arrivals on blended data directly is challenging. The direct arrivals for blended data can be picked effectively after applying pseudodeblending. Note that a similar technique can be extended to use VSP data acquired onshore. However, in land data, there will be other processing aspects to be taken care of such as near-surface issues and statics.

We have also used an acoustic finite-difference scheme to simulate our measured data, and the discussed inversion scheme is restricted to handle only PP reflections. Including the converted wavefields to estimate full elastic reflectivities is the subject of current research. If we use an elastic finite-difference scheme to generate our data, we expect to see higher residuals in the current algorithm, in which the residuals include the converted waves in the measured data.

The current illustrations are limited to 2D cases. The reformulation of the algorithm to the full 3D case, based on the same concepts, should be possible if the sampling of sources at the surface is dense enough to provide proper 3D wavefield extrapolation. Because of the inversion approach in the FWM method, some flexibility regarding incomplete source sampling is expected to be present. A first report on 3D FWM for VSP data is given by El-Marhfoul and Verschuur (2014). Finally, for application to a real data case, a basic preprocessing sequence is required to handle

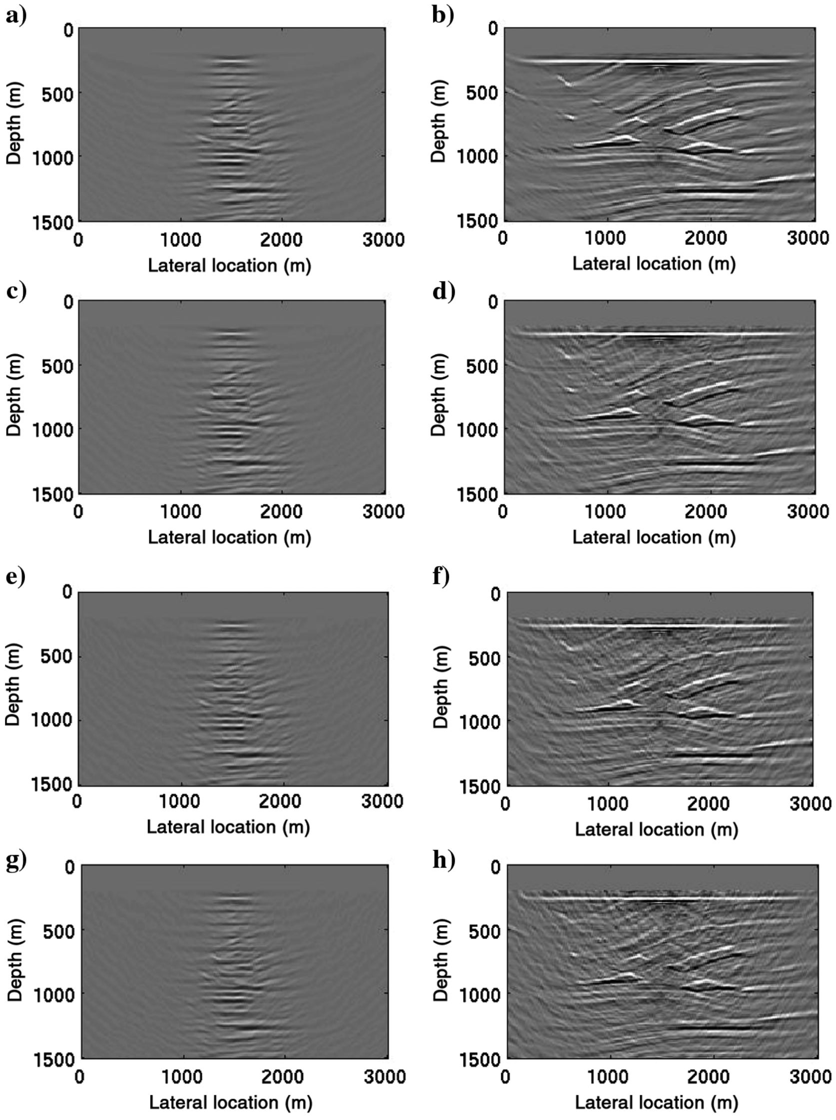

Figure 15. Image comparison after the first and tenth iteration of FWM on blended VSP data with different blending factors. Panels (a, c, e, and g) show the image after the first iteration of FWM using blended VSP data with blending factors one, two, three, and four, respectively; panels (b, d, f, and h) show the image after the tenth iteration of FWM using blended VSP data with blending factors of one, two, three, and four, respectively.

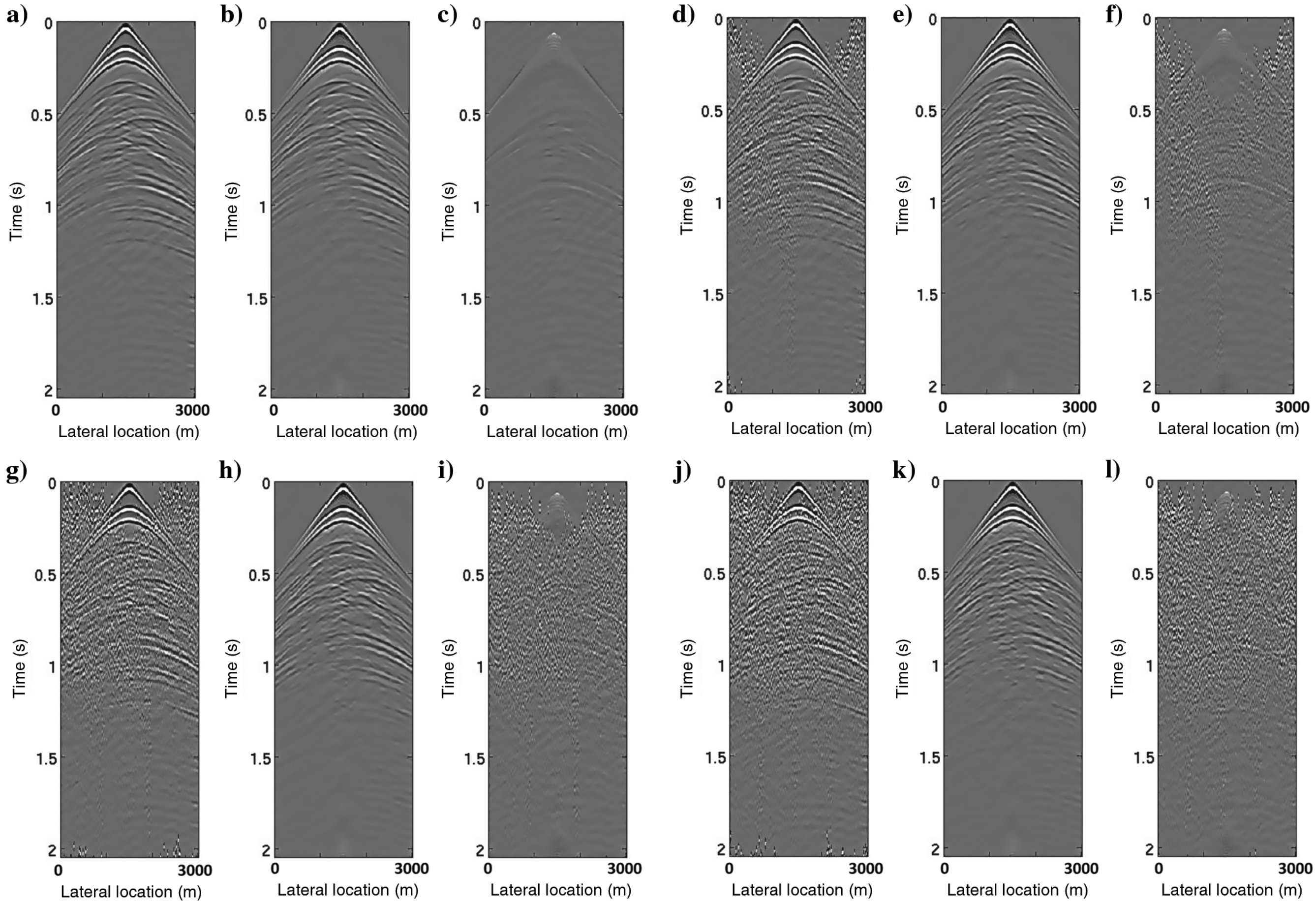

Figure 16. The 2D Marmousi model: comparison of pseudodeblended observed data, estimated unblended data, and their difference, after the twentieth iteration of FWM on the blended VSP data with different blending factors. Panels (a, d, g, and j) show an example pseudodeblended observed or measured common-receiver gather for blending factors of one, two, three, and four, respectively; panels (b, e, h, and k) show the corresponding estimated unblended common-receiver gather for blending factors of one, two, three, and four, respectively; and panels (c, f, i, and l) show the corresponding difference for blending factors of one, two, three, and four , respectively. Note the increase in the blending noise with increase in blending factor. Also, note how the imaging process helps to separate the randomized noise from the coherent events.

issues such as tube waves, other random noise, geometry, and coupling errors.

CONCLUSIONS

We have proposed the FWM approach to directly image blended VSP data in which the forward-modeling process includes the blended source experiments. We have illustrated the iterative modeling scheme and shown how the complex, higher-order scattering (i.e., the multiples) can be built iteratively using the reflectivity image. Furthermore, the inversion scheme for FWM is illustrated using a numerical example for blending factors of one, two, three, and four. We clearly see that using the primaries, surface multiples, and internal multiples enhances the illumination away from the well trajectory. Also, the algorithm handles the blended data effectively, without the need of an active deblending step in preprocessing. We have also illustrated that an unconstrained least-squares inversion scheme in FWM can yield reasonable images even for high blending factors. However, we do see more blending crosstalk noise leaking into the image for data acquired with higher blending factors. We expect that a constrained inversion can help further suppress the crosstalk noise from the image.

ACKNOWLEDGMENTS

The authors thank the sponsoring companies of the Delphi Research Consortium for their support. Special thanks are due to A. J. Berkhout for many fruitful discussions. Also, many thanks are due to A. Guitton, I. Moore, and two anonymous reviewers for their contributions that helped improve this paper.

APPENDIX A

THE INVERSION SCHEME

As discussed in the “FWM of blended VSP data” section, we formulate the problem as a least-squares inversion scheme. The objective function to be minimized can be written as

$$J = \sum_k \sum_\omega \|\vec{P}^-_{\text{bl,obs},k} - \vec{P}^-_{\text{bl,est},k}\|^2_2, \tag{A-1}$$

where $\vec{P}_{\text{bl,obs}}$ and $\vec{P}_{\text{bl,est}}$ are the observed and the estimated blended VSP data. The subscript k is for the kth blended source experiment. In equation A-1, the estimated blended VSP data at the surface can be computed using equations 9 and 10 as

$$\begin{aligned}\vec{P}^{-T}_{\text{bl,est}} &= \Gamma^T_{\text{bl}} \sum_{m=0}^{N} \mathbf{W}^-(z_n, z_m)[\delta\vec{P}(z_m)^{(i-1)} + \vec{S}^-(z_m)] \\ &= \Gamma^T_{\text{bl}} \vec{P}^{-T}_{\text{est}},\end{aligned} \tag{A-2}$$

where $\vec{S}^-$ is the upgoing source wavefield located in the borehole in the reciprocal domain. Note that in the inversion scheme, the first step is to estimate the source wavefield using the picked direct arrivals. The two-way scattered wavefield $\delta\vec{P}(z_n)$ is the function of the reflectivity matrix and is described by equation 5. Furthermore, the blended residual $\vec{E}_{\text{bl},k}$ that we aim to minimize is given by

$$\vec{E}_{\text{bl},k} = \vec{P}^-_{\text{bl,obs},k} - \vec{P}^-_{\text{bl,est},k}. \tag{A-3}$$

We know that in the common-receiver domain, the blended residual is randomized. Therefore, we cannot input the blended residual directly into our imaging scheme. However, for imaging in the common-receiver domain, we perform an intermediate pseudodeblending (also called *passive deblending*) of the residual. Using equation 13, the pseudodeblending of the residual can be written as

$$\vec{E}_k = \frac{1}{b} \vec{E}_{\text{bl}} \Gamma^H_{\text{bl}}. \tag{A-4}$$

Figure A-1 demonstrates pseudodeblending of residual data in FWM at the first iteration, i.e., when the residual is the same as the input measured blended VSP data. Note that pseudodeblending is not a perfect inversion scheme; therefore, deblended data do have blending noise or interference. In the case of pseudodeblending, the data are copied N_{bl} (blending factor) times, followed by the time shift (decoded) to undo the time shift introduced during data acquisition. The interference noise occurs because the source codes are not orthogonal and the single deblended gather still includes contribution from multiple shots (Mahdad et al., 2011b).

Furthermore, the gradient of the objective function is computed with respect to the subsurface reflectivity. To compute the gradient, we use the zero-lag correlation between the back-projected pseudodeblended residual and the forward-propagated downgoing wavefields (for more details, see, e.g., Tarantola, 1984, 1987). The steepest-descent direction is the negative of the gradient and can be written for a depth level z_n as (Soni and Verschuur, 2014a)

$$\Delta\mathbf{R}^\cup(z_n) = -\sum_k [\mathbf{W}^-(z_0, z_n)]^H \vec{E}_k(z_0)[\vec{P}^+_k(z_n)]^H. \tag{A-5}$$

Note that we only use the downgoing $\vec{P}^+(z_n)$ wavefield instead of the total $\vec{P}(z_n)$ wavefield in the gradient computation, which helps in avoiding the crosstalk artifacts due to transmission effects.

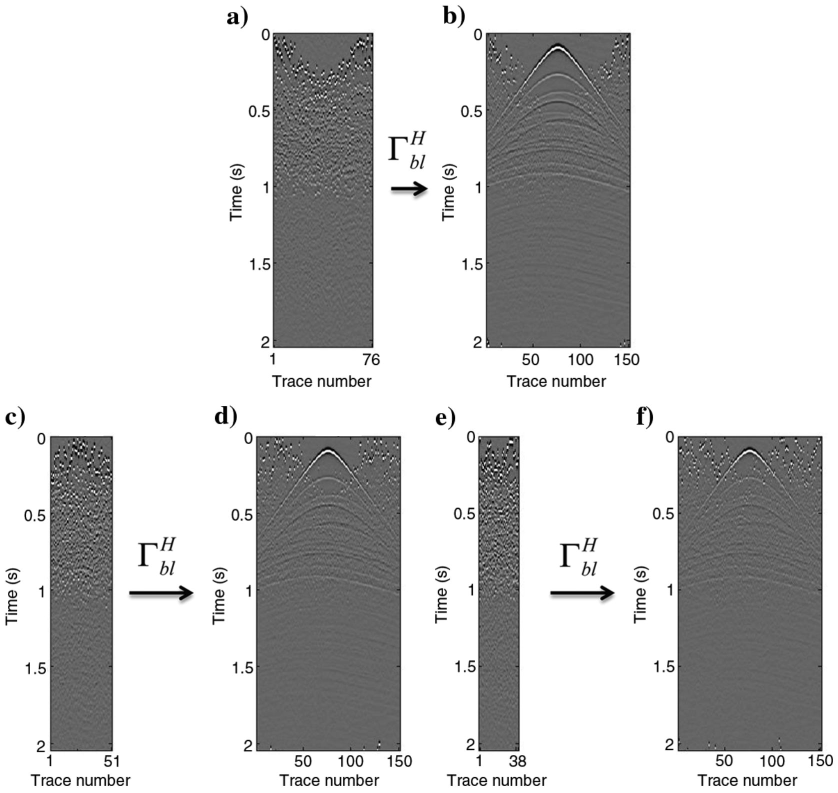

Figure A-1. Demonstration of pseudodeblending of residual data in FWM at the first iteration, i.e., when the residual is the same as the input measured blended VSP data. Panels (a, c, and e) show an example blended common-receiver domain residual data for blending factors of two, three, and four, respectively. Panels (b, d, and f) show an example pseudodeblended common-receiver domain residual data for blending factors of two, three, and four, respectively.

Algorithm A-1. Pseudocode for the FWM algorithm using an iterative conjugate-gradient scheme to image blended VSP data in common-receiver domain.

```
initialization: $\mathbf{R}^{(0)} = 0$, $\vec{E}_{\mathrm{bl},k} = \vec{P}^{T}_{\mathrm{bl,obs},k}$, $i = 1$
while $i \leq i_{\max}$ AND $|\vec{E}_{\mathrm{bl},k}| > |\vec{E}_{\mathrm{tolerance}}|$
compute $\vec{P}_{k}^{+(i)}$, $\vec{P}_{k}^{-(i)}$ for all sources $k$, at all depth levels
estimate unblended $\vec{P}^{T}_{\mathrm{est},k}$ at the surface
blend the estimated data at the surface $\vec{P}^{T}_{\mathrm{est},k} = \Gamma^{T}_{\mathrm{bl}}\vec{P}^{T}_{\mathrm{est},k}$
blended data misfit $\vec{E}_{\mathrm{bl},k} = \vec{P}^{T}_{\mathrm{bl,obs},k} - \vec{P}^{T}_{\mathrm{bl,est},k}$
pseudodeblended data misfit $\vec{E}_{k} = \frac{1}{b}\vec{E}_{k}\Gamma^{H}_{\mathrm{bl}}$
compute gradient $\Delta\mathbf{R}^{\cup(i)}$ for all depth levels
if $i = 1$
$\beta^{(i)} = 0$
else
$\beta^{(i)} = \Delta\mathbf{R}^{(i)H}[\Delta\mathbf{R}^{(i)} - \Delta\mathbf{R}^{(i-1)}]/[\Delta\mathbf{R}^{(i-1)H}\Delta\mathbf{R}^{(i-1)}]$
estimate the conjugate direction $\Delta\mathbf{R}^{\cup(i)}_{\mathrm{cg}} = \Delta\mathbf{R}^{\cup(i)} + \beta^{(i)}\Delta\mathbf{R}^{\cup(i-1)}_{\mathrm{cg}}$
search for $\alpha^{(i)}$, $\alpha^{(i)} = arg\min_{\alpha}[J(\mathbf{R}^{\cup(i-1)} + \alpha^{(i)}\Delta\mathbf{R}^{\cup(i)}_{\mathrm{cg}})]$
update the reflectivity matrix $\mathbf{R}^{(i)} = \mathbf{R}^{(i-1)} + \alpha^{(i)}\Delta\mathbf{R}^{\cup(i)}_{\mathrm{cg}}$
$i = i + 1$
```

Further, in the CG scheme, the new search direction is made orthogonal to the previous gradient using the gradients of two consecutive iterations i and $i-1$. We have used the Polak-Ribiere algorithm (Polak and Ribiere, 1969) to update the search direction. Further, at any iteration i, the update can be computed by finding the appropriate step length α in the gradient scheme as

$$\mathbf{R}^{\cup(i)} = \mathbf{R}^{\cup(i-1)} + \alpha^{(i-1)}\Delta\mathbf{R}^{\cup(i-1)}_{cg}, \tag{A-6}$$

such that objective function J is minimized, and $\Delta\mathbf{R}^{\cup(i-1)}_{\mathrm{cg}}$ is the computed conjugate direction. We perform the iteration until the estimated reflectivity image explains the total measured data; i.e., the residual goes below a predefined level of error tolerance or until a predefined maximum number of iterations is exceeded assuming that the convergence becomes very slow beyond that iteration. In Algorithm A-1, the pseudocode of the FWM inversion algorithm for blended VSP data using conjugate gradient scheme is given.

REFERENCES

Ayeni, G., A. Almomin, and D. Nichols, 2011, On the separation of simultaneous-source data by inversion: 81st Annual International Meeting, SEG, Expanded Abstracts, 20–25.

Ayeni, G., Y. Tang, and B. Biondi, 2009, Joint preconditioned least-squares inversion of simultaneous source time-lapse seismic data sets: 79th Annual International Meeting, SEG, Expanded Abstracts, 3914–3918.

Bagaini, C., 2006, Overview of simultaneous vibroseis acquisition methods: 66th Annual International Meeting, SEG, Expanded Abstracts, 70–74.

Bagaini, C., M. Daly, and I. Moore, 2012, The acquisition and processing of dithered slip-sweep vibroseis data: Geophysical Prospecting, **60**, 618–639, doi: 10.1111/j.1365-2478.2012.01085.x.

Beasley, C. J., R. E. Chambers, and Z. Jiang, 1998, A new look at simultaneous sources: 68th Annual International Meeting, SEG, Expanded Abstracts, 133–135.

Beasley, C. J., B. Dragoset, and A. Salama, 2012, A 3D simultaneous source field test processed using alternating projections: A new active separation method: Geophysical Prospecting, **60**, 591–601, doi: 10.1111/j.1365-2478.2011.01038.x.

Berkhout, A. J., 2008, Changing the mindset in seismic acquisition: The Leading Edge, **27**, 924–938, doi: 10.1190/1.2954035.

Berkhout, A. J., 2012, Combining full wavefield migration and full waveform inversion: Geophysics, **77**, no. 2, S43–S50, doi: 10.1190/geo2011-0148.1.

Berkhout, A. J., 2014a, Review paper: An outlook on the future seismic imaging — Part1: Forward and reverse modelling: Geophysical Prospecting, **62**, 911–930, doi: 10.1111/1365-2478.12161.

Berkhout, A. J., 2014b, Review paper: An outlook on the future seismic imaging — Part2: Full-wavefield migration: Geophysical Prospecting, **62**, 931–949, doi: 10.1111/1365-2478.12154.

Berkhout, A. J., 2014c, Review paper: An outlook on the future seismic imaging — Part3: Joint migration inversion: Geophysical Prospecting, **62**, 950–971, doi: 10.1111/1365-2478.12158.

Berkhout, A. J., G. Blacquiere, and D. J. Verschuur, 2008, From simultaneous shooting to blended acquisition: 78th Annual International Meeting, SEG, Expanded Abstracts, 2831–2838.

Berkhout, A. J., G. Blacquiere, and D. J. Verschuur, 2009, The concept of double blending: Combining incoherent shooting with incoherent sensing: Geophysics, **74**, no. 4, A59–A62, doi: 10.1190/1.3141895.

Berkhout, A. J., and D. J. Verschuur, 2011, Full wavefield migration, utilizing surface and internal multiple scattering: 81st Annual International Meeting, SEG, Expanded Abstracts, 3212–3216.

Berkhout, A. J., D. J. Verschuur, and G. Blacquiere, 2012, Illumination properties and imaging promises of blended, multiple-scattering seismic data: A tutorial: Geophysical Prospecting, **60**, 713–732, doi: 10.1111/j.1365-2478.2012.01081.x.

Blacquiere, G., A. J. Berkhout, and D. J. Verschuur, 2009, Survey design for blended acquisition: 79th Annual International Meeting, SEG, Expanded Abstracts, 56–60.

Bouska, J., 2010, Distance separated simultaneous sweeping, for fast, clean, vibroseis acquisition: Geophysical Prospecting, **58**, 123–153, doi: 10.1111/j.1365-2478.2009.00843.x.

Choi, Y., and T. Alkhalifah, 2012, Application of multi-source waveform inversion to marine streamer data using the global correlation norm: Geophysical Prospecting, **60**, 748–758, doi: 10.1111/j.1365-2478.2012.01079.x.

Claerbout, J. F., 1976, Fundamental of geophysical data processing: Blackwell Scientific Publications.

Dai, W., P. Fowler, and G. T. Schuster, 2012, Multi-source least-squares reverse time migration: Geophysical Prospecting, **60**, 681–695, doi: 10.1111/j.1365-2478.2012.01092.x.

Davydenko, M., X. R. Staal, and D. J. Verschuur, 2012, Full wavefield migration in multidimensional media: 82nd Annual International Meeting, SEG, Expanded Abstracts, doi: 10.1190/segam2012-1583.1.

Davydenko, M., and D. J. Verschuur, 2013, Full wavefield migration without dip limitation — Using duplex waves in the imaging with multiples: 75th Annual International Conference and Exhibition, EAGE, Extended Abstracts, We P02 09.

Davydenko, M., and D. J. Verschuur, 2014, Omnidirectional extension of full wavefield migration: 76th Annual International Conference and Exhibition, EAGE, Extended Abstracts, Tu G103 06.

de Bruin, C. G. M., C. P. A. Wapenaar, and A. J. Berkhout, 1990, Angle-dependent reflectivity by means of prestack migration: Geophysics, **55**, 1223–1234, doi: 10.1190/1.1442938.

Doulgeris, P., 2013, Inversion methods for separation of blended data: Ph.D. thesis, Delft University of Technology.

Doulgeris, P., K. Bube, G. Hampson, and G. Blacquiere, 2012, Convergence analysis of a coherency-constrained inversion for the separation of blended data: Geophysical Prospecting, **60**, 769–781, doi: 10.1111/j.1365-2478.2012.01088.x.

Doulgeris, P., A. Mahdad, and G. Blacquiere, 2011, Iterative separation of blended marine data: Discussion on the coherence-pass filter: 81st Annual International Meeting, SEG, Extended Abstracts, 26–31.

El-Marhfoul, B., and D. J. Verschuur, 2014, 3D joint full wavefield migration of surface and VSP data: 84th Annual International Meeting, SEG, Expanded Abstracts, 5070–5074.

Ghazali, A. R., D. J. Verschuur, and A. Gisolf, 2010, Multi-dimensional nonlinear full waveform inversion of gas cloud reflection data using a genetic algorithm and a blended acquisition approach: 80th Annual International Meeting, SEG, Expanded Abstracts, 935–939.

Godwin, J., and P. Sava, 2013, A comparison of shot-encoding schemes for wave-equation migration: Geophysical Prospecting, **61**, 391–408, doi: 10.1111/j.1365-2478.2013.01125.x.

Guitton, A., and E. Diaz, 2012, Attenuating crosstalk noise with simultaneous source full waveform inversion: Geophysical Prospecting, **60**, 759–768, doi: 10.1111/j.1365-2478.2011.01023.x.

Gulati, J. S., A. Salama, S. W. Leaney, C. J. Beasley, E. Coste, H. Menkiti, and J. Tulett, 2011, Faster 3D VSP acquisition using simultaneous sources: 81st Annual International Meeting, SEG, Expanded Abstracts, 4249–4252.

Hestenes, M. R., and E. Stiefel, 1952, Methods of conjugate gradients for solving linear systems: Journal of Research of the National Bureau of Standards, **49**, 409–436, doi: 10.6028/jres.049.044.

Hou, S., C. Tsingas, P. G. Kelamis, P. I. Pecholcs, and H. Xu, 2012, Unconstrained simultaneous source land data processing: Geophysical Prospecting, **60**, 608–617, doi: 10.1111/j.1365-2478.2012.01074.x.

Howe, D., M. Foster, T. Allen, B. Taylor, and I. Jack, 2008, Independent simultaneous sweeping a method to increase the productivity of land seismic crews: 78th Annual International Meeting, SEG, Expanded Abstracts, 2826–2830.

Huang, Y., and G. T. Schuster, 2012, Multi-source least-squares migration of marine streamer and land data with frequency-division encoding: Geophysical Prospecting, **60**, 663–680, doi: 10.1111/j.1365-2478.2012.01086.x.

Huo, S., Y. Luo, and P. Kelamis, 2009, Simultaneous sources separation via multi-directional vector-median filter: 79th Annual International Meeting, SEG, Expanded Abstracts, 31–35.

Ikelle, L. T., 2007, Coding and decoding: Seismic data modeling, acquisition and processing: 77th Annual International Meeting, SEG, Expanded Abstracts, 66–70.

Jiang, Z., and R. Abma, 2010, An analysis on the simultaneous imaging of simultaneous source data: 80th Annual International Meeting, SEG, Expanded Abstracts, 3115–3119.

Kennett, B. L. N., 1979, Theoretical reflection seismograms for elastic media: Geophysical Prospecting, **27**, 301–321, doi: 10.1111/j.1365-2478.1979.tb00972.x.

Kim, Y., I. Gruzinov, M. Guo, and S. Sen, 2009, Source separation of simultaneous source OBC data: 79th Annual International Meeting, SEG, Expanded Abstracts, 51–55.

Mahdad, A., 2012, Deblending of seismic data: Ph.D. thesis, Delft University of Technology.

Mahdad, A., P. Doulgeris, and G. Blacquiere, 2011a, Separation of blended data by iterative estimation and subtraction of blending interference noise: Geophysics, **76**, no.3, Q9–Q17, doi: 10.1190/1.3556597.

Mahdad, A., P. Doulgeris, and G. Blacquiere, 2011b, Separation of blended data by iterative estimation and subtraction of blending interference noise: Geophysics, **76**, no. 3, Q9–Q17, doi: 10.1190/1.3556597.

Mahdad, A., P. Doulgeris, and G. Blacquiere, 2012, Iterative method for the separation of blended seismic data: Discussion on the algorithmic aspects: Geophysical Prospecting, **60**, 782–801, doi: 10.1111/j.1365-2478.2012.01084.x.

Moore, I., W. Dragoset, T. Ommundsen, D. Wilson, C. Ward, and D. Eke, 2008, Simultaneous source separation using dithered sources: 78th Annual International Meeting, SEG, Expanded abstracts, 2806–2809.

Morley, L. C., 2013, Application of compressive sensing to 3D-VSP acquisition and processing: 75th Annual International Conference and Exhibition, EAGE, Extended Abstracts, BG14.

Nawaz, M. A., and W. H. Borland, 2013, Simulation and proposed processing workflow of simultaneous source 3D-VSP data: 75th Annual International Conference and Exhibition, EAGE, Extended Abstracts, BG27.

Nemeth, T., C. Wu, and G. T. Schuster, 1999, Least-squares migration of incomplete reflection data: Geophysics, **64**, 208–221, doi: 10.1190/1.1444517.

Plessix, R. E., G. Beeten, J. W. de Maag, F. ten Kroode, and Z. Ruijie, 2012, Full waveform inversion and distance separated simultaneous sweeping: A study with a land seismic data set: Geophysical Prospecting, **60**, 733–747, doi: 10.1111/j.1365-2478.2011.01036.x.

Polak, E., and G. Ribiere, 1969, Note sur la convergence de directions conjuges: Revue Française d'Informatique et de Recherche Opérationnelle, **16**, 35–43.

Routh, P., J. Krebs, S. Lazaratos, A. Baumstein, S. Lee, Y. H. Cha, I. Chikichev, N. Downey, D. Hinkley, and J. Anderson, 2011, Encoded simultaneous source full-wavefield inversion for spectrally shaped marine streamer data: 81st Annual International Meeting, SEG, Expanded Abstracts, 2433–2438.

Soni, A. K., X. R. Staal, and D. J. Verschuur, 2012, VSP imaging using all multiples: Full wavefield migration approach: 82nd Annual International Meeting, SEG, Expanded Abstracts, doi: 10.1190/segam2012-0695.1.

Soni, A. K., and D. J. Verschuur, 2013a, Full wavefield migration of vertical seismic profiling data: Using all multiples for imaging away from the well: 75th Annual International Conference and Exhibition, EAGE, Extended Abstracts, BG10.

Soni, A. K., and D. J. Verschuur, 2013b, Imaging blended VSP data using full wavefield migration: 83rd Annual International Meeting, SEG, Expanded Abstracts, 5046–5051.

Soni, A. K., and D. J. Verschuur, 2013c, Imaging vertical seismic profiling data using full wavefield migration: 75th Annual International Conference and Exhibition, EAGE, Extended Abstracts, Th 17 11.

Soni, A. K., and D. J. Verschuur, 2014a, Imaging of blended VSP data using full wavefield migration in the common-receiver domain: 76th Annual International Conference and Exhibition, EAGE, Expanded Abstracts, Tu G102 15.

Soni, A. K., and D. J. Verschuur, 2014b, Full wavefield migration of vertical seismic profiling data: Using all multiples to extend the illumination area: Geophysical Prospecting, **62**, 740–759, doi: 10.1111/1365-2478.12130.

Soni, A. K., D. J. Verschuur, and M. Davydenko, 2014, Full wavefield migration to image salt- flanks using an unblended and blended VSP data: 84th Annual International Meeting, SEG, Extended Abstracts, 5085–5091.

Spitz, S., G. Hampson, and A. Pica, 2008, Simultaneous source separation: A prediction- subtraction approach: 78th Annual International Meeting, SEG, Expanded Abstracts, 2811–2814.

Staal, X. R., and D. J. Verschuur, 2012, Velocity estimation using internal multiples: 82nd Annual International Meeting, SEG, Expanded Abstracts, doi: 10.1190/segam2012-1580.1.

Staal, X. R., and D. J. Verschuur, 2013, Joint migration inversion, imaging including all multiples with automatic velocity update: 75th Annual International Conference and Exhibition, EAGE, Extended Abstracts, Tu 0106.

Staal, X. R., D. J. Verschuur, and A. J. Berkhout, 2014, Robust velocity estimation by joint migration inversion: 76th Annual International Conference and Exhibition, EAGE, Extended Abstracts, We G103 07.

Stefani, J., G. Hampson, and E. F. Herkenhoff, 2007, Acquisition using simultaneous sources: 69th Annual International Conference and Exhibition, EAGE, Extended Abstracts, B006.

Tang, Y., and B. Biondi, 2009, Least-squares migration/inversion of blended data: 79th Annual International Meeting, SEG, Expanded Abstracts, 2859–2863.

Tarantola, A., 1984, Inversion of seismic reflection data in the acoustic approximation: Geophysics, **49**, 1259–1266., doi: 10.1190/1.1441754.

Tarantola, A., 1987, Inverse problem theory, methods for data fitting and model parameter estimation: Elsevier Science Publication Co., Inc.

Thorbecke, J. W., K. Wapenaar, and G. Swinnen, 2004, Design of one-way wavefield extrapolation operators, using smooth functions in WLSQ optimization: Geophysics, **69**, 1037–1045, doi: 10.1190/1.1778246.

van Borselen, R., R. Baardman, T. Martin, B. Goswami, and E. Fromyr, 2012, An inversion approach to separating sources in marine simultaneous shooting acquisition — Application to a Gulf of Mexico data set: Geophysical Prospecting, **60**, 640–647, doi: 10.1111/j.1365-2478.2012.01076.x.

van Groenestijn, G. J. A., and D. J. Verschuur, 2011, Using surface multiples to estimate primaries by sparse inversion from blended data: Geophysical Prospecting, **59**, 10–23, doi: 10.1111/j.1365-2478.2010.00894.x.

Verschuur, D. J., and A. J. Berkhout, 2009, Target-oriented, least-squares imaging of blended data: 79th Annual International Meeting, SEG, Expanded Abstracts, 2889–2893.

Verschuur, D. J., and A. J. Berkhout, 2011, Seismic migration of blended shot records with surface-related multiple scattering: Geophysics, **76**, no. 1, A7–A13, doi: 10.1190/1.3521658.

Wapenaar, K., J. van der Neut, and J. Thorbecke, 2012, Deblending by direct inversion: Geophysics, **77**, no. 3, A9–A12, doi: 10.1190/geo2011-0497.1.